Ensemble Kalman Filter Data Assimilation in a 1D Numerical Model Used for Fog Forecasting

SAMUEL RÉMY AND THIERRY BERGOT

CNRM/GAME, Toulouse, France

(Manuscript received 22 June 2009, in final form 21 September 2009)

ABSTRACT

Because poor visibility conditions have a considerable influence on airport traffic, a need exists for accurate and updated fog and low-cloud forecasts. Couche Brouillard Eau Liquide (COBEL)-Interactions between Soil, Biosphere, and Atmosphere (ISBA), a boundary layer 1D numerical model, has been developed for the very short-term forecast of fog and low clouds. This forecast system assimilates local observations to produce initial profiles of temperature and specific humidity. The initial conditions have a great impact on the skill of the forecast.

In this work, the authors first estimated the background error statistics; they varied greatly with time, and cross correlations between temperature and humidity in the background were significant. This led to the implementation of an ensemble Kalman filter (EnKF) within COBEL-ISBA. The new assimilation system was evaluated with temperature and specific humidity scores, as well as in terms of its impact on the quality of fog forecasts. Simulated observations were used and focused on the modeling of the atmosphere before fog formation and also on the simulation of the life cycle of fog and low clouds. For both situations, the EnKF brought a significant improvement in the initial conditions and the forecasts. The forecast of the onset and burn-off times of fogs was also improved. The EnKF was also tested with real observations and gave good results. The size of the ensemble did not have much impact when simulated observations were used, thanks to an adaptive covariance inflation algorithm, but the impact was greater when real observations were used.

1. Introduction

Low-visibility conditions often cause problems at many international airports. Such conditions may reduce the landing–takeoff traffic by a factor of 2, leading to delays or even cancellations of flights. This is why accurate forecasts of these conditions have become an important issue. Each airport defines a set of visibility and ceiling thresholds below which safety procedures, called low-visibility procedures (LVP), are applied. At the Paris, France, Charles De Gaulle Airport, the threshold values are set at 600 m for visibility and 60 m for the ceiling.

Various approaches are employed to forecast low-visibility conditions. For airports located in flat terrain, 1D models are suitable for the nowcasting of radiation fog events (Bergot and Guédalia 1994a,b). They are currently used in real time to forecast fog at the local scale (e.g., Clark 2002, 2006; Herzegh et al. 2003). The 1D boundary layer model Couche Brouillard Eau Liquide (COBEL), coupled with the land surface scheme Interactions between Soil, Biosphere, and Atmosphere (ISBA; as documented in Bergot et al. 2005) has been in operational use since 2005 at Charles de Gaulle Airport to provide estimated times for the onset and lifting of LVP conditions.

Fog is a phenomenon that evolves at small spatial and time scales. Its 1D modeling involves interactions between many parameterizations: turbulence, microphysics, radiative scheme, and surface–atmosphere exchanges. This highlights the importance of working with accurate initial conditions because the quality of the COBEL-ISBA forecasts is dependent on the initial conditions (Bergot and Guédalia 1994a; Roquelaure and Bergot 2007; Rémy and Bergot 2009). This paper aims to improve fog forecasting by using an ensemble Kalman filter (EnKF; Evensen 1994, 2003). Theoretically, ensemble filters are an adequate method for taking the atmosphere variability into account in the assimilation scheme of nonlinear systems, such as boundary layer 1D models. They have recently been implemented in

Corresponding author address: Samuel Rémy, CNRM/GAME, 2 Ave. Rapp, 75340 Paris CEDEX 07, France.
E-mail: samuel.remy@meteo.fr

DOI: 10.1175/2009MWR3110.1

various oceanic and atmospheric models (Houtekamer et al. 2005; Zhang 2005; Hacker and Snyder 2005; Hacker and Rostkier-Edelstein 2007; among others). Here, an implementation of this method for 1D fog forecasts is presented, using both model simulated and real observations.

The framework of this study is outlined in section 2. Two sets of simulated observations were created: one with mostly clear-sky conditions at the initialization, to study the formation of fog, and the other with frequent occurrence of fog and low clouds. Section 3 presents the setup of the EnKF, and section 4 shows the results with the two sets of simulated observations. Next, in section 5, we focus on results obtained from a system using real observations instead of simulated ones. In section 6, the impact of the ensemble size on the performance of the EnKF, for simulated and real observations, is discussed. Finally, section 7 summarizes the results.

2. Framework of the study

a. The COBEL-ISBA assimilation prediction system

1) THE MODEL

COBEL-ISBA consists of the coupling of the high-resolution atmospheric boundary layer 1D model COBEL (Bergot 1993; Bergot and Guédalia 1994a,b) with the seven-layer land surface scheme ISBA (Noilhan and Planton 1989; Boone 2000). To be able to adequately forecast radiative fog events, it possesses a high vertical resolution: 30 levels between 0.5 and 1360 m, with 20 levels below 200 m. The physical parameterizations used in COBEL-ISBA consist of

- a turbulent mixing scheme with a 1.5-order turbulence closure that uses a prognostic turbulent kinetic energy (TKE) equation. The mixing length differs for stable (Estournel 1988) and for neutral or unstable conditions (Bougeault and Lacarrere 1989);
- a warm microphysical scheme adapted to fog and low clouds in temperate regions; and
- detailed longwave and shortwave radiation transfer schemes.

COBEL-ISBA is run at 1-h intervals and provides up to 8 h of LVP forecasts. The inputs of the model are the initial conditions and mesoscale forcings. Mesoscale forcings (i.e., geostrophic wind, horizontal advection, and cloud cover above the model column) are given by the Numerical Weather Prediction (NWP) model Aire Limitée Adaptation Dynamique Développement International (ALADIN, available online at http://www.cnrm-game-meteo.fr/aladin/).

2) THE ASSIMILATION SCHEME

The initial conditions are given by a two-step assimilation scheme, using local observations (Bergot et al. 2005). The observation system used at the Charles de Gaulle Airport is designed to provide up-to-date information on the state of the surface boundary layer temperature and moisture. It includes a weather station that provides 2-m temperature and humidity; visibility and ceiling; a measurement mast that gives temperature and humidity observations at 1, 5, 10, and 30 m; radiative fluxes (shortwave and longwave) observations at 2 and 45 m; and soil temperature and water content between the surface and −40 cm.

The assimilation system uses information from a first guess or background (i.e., a previous 1-h COBEL-ISBA forecast), local observations, and profiles from the ALADIN NWP model to generate a best linear unbiased estimator (BLUE) for initial conditions of temperature and specific humidity:

$$x^a = x^b + \mathbf{K}(y^o - \mathbf{H}x^b) \quad \text{and} \tag{1}$$

$$\mathbf{K} = \mathbf{B}\mathbf{H}^{\mathrm{T}}(\mathbf{H}\mathbf{B}\mathbf{H}^{\mathrm{T}} + \mathbf{R})^{-1}. \tag{2}$$

In this equation x^a is the analysis, x^b is the first guess or background, y^o are the observations, $\mathbf{K}$ is the Kalman gain that accomplishes the observation weighting, $\mathbf{B}$ and $\mathbf{R}$ are the error variance and covariance matrices of the background and of the observations, and $\mathbf{H}$ is the forward operator—that is, the matrix that interpolates information from the model grid to the observation grid. Because the dimension of the system is low, matrices can be explicitly inverted and there is no need for a variational algorithm. The ALADIN data are taken as observations for the upper levels of the model domain, so a part of $\mathbf{R}$ corresponds to the error variances and covariances of the ALADIN profiles. The covariances between the other observations are zero. In the operational setup, the error statistics are imposed arbitrarily to allow the initial profile to be close to observations near the surface and closer to the ALADIN profiles above. The cross correlation of temperature and humidity errors in the background are zero, and the operational assimilation scheme is monovariate. Our objective is to compute flow-dependent background error statistics and to build a multivariate assimilation scheme by taking into account the cross correlations of temperature and humidity errors in the background.

When a layer of cloud is detected, an additional step uses a minimization algorithm together with measurement of radiative fluxes at the ground and at 45 m to estimate cloud thickness. The radiation scheme of COBEL

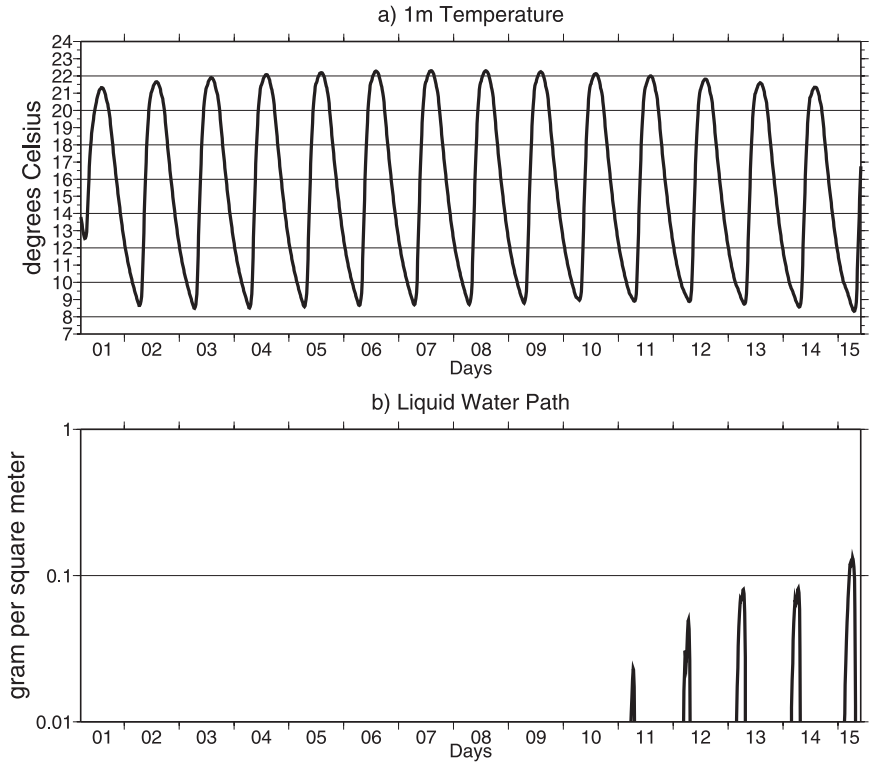

FIG. 1. "Truth" for (a) 1-m temperature and (b) liquid water path for NEAR-FOG.

is used to compute the modeled radiative fluxes at 2 and 45 m, using different initial thicknesses of the fog layer. The best estimate of the initial fog thickness is the one that minimizes the error between modeled and observed radiative fluxes (see Bergot et al. 2005 for more details). The relative humidity profile is then modified within the saturated layer.

The soil temperature and water content profiles used to initialize ISBA are obtained directly by interpolation of soil measurements.

b. Simulated observations

The Observing System Simulation Experiment (OSSE) is adequate to study the accuracy of an assimilation scheme (e.g., Huang et al. 2007). It consists of generating pseudo-observations by adding perturbations to a reference run of the model. The pseudo-observations are then assimilated, and the initial state and forecast can be compared to the reference run. The advantages of this method are as follows:

- The same physical processes are underlying both observations and simulations, which leads to the fact that there are no modeling errors. The only source of error when using simulated observations are the initial conditions, which is why they are used often in data assimilation studies. The errors in the initial conditions originate only in the observations and first-guess errors, themselves originating from errors in initial conditions propagated by the previous forecast. The lack of observations for certain parameters (e.g., the thickness or water content of a cloud layer) does not allow the assimilation scheme to entirely correct the errors of the first-guess field. The quality of initial conditions thus depends solely on the observations used and on the assimilation scheme.
- The framework provides the simulated observation for the entire domain of COBEL-ISBA.
- Last, it is possible to create a large variety of observation sets that accommodate our needs for evaluation purposes.

The perturbations added to the reference run were all independent from each other, meaning that the errors of the ALADIN profiles at different levels are uncorrelated, which is not the case when using real observations. When using simulated observations, the **R** matrix is thus completely diagonal.

There are two sets of simulated observations: one for the study of clear-sky night and shallow-fog situations (NEAR-FOG); and the other for the study of frequent deep fogs (FOG).

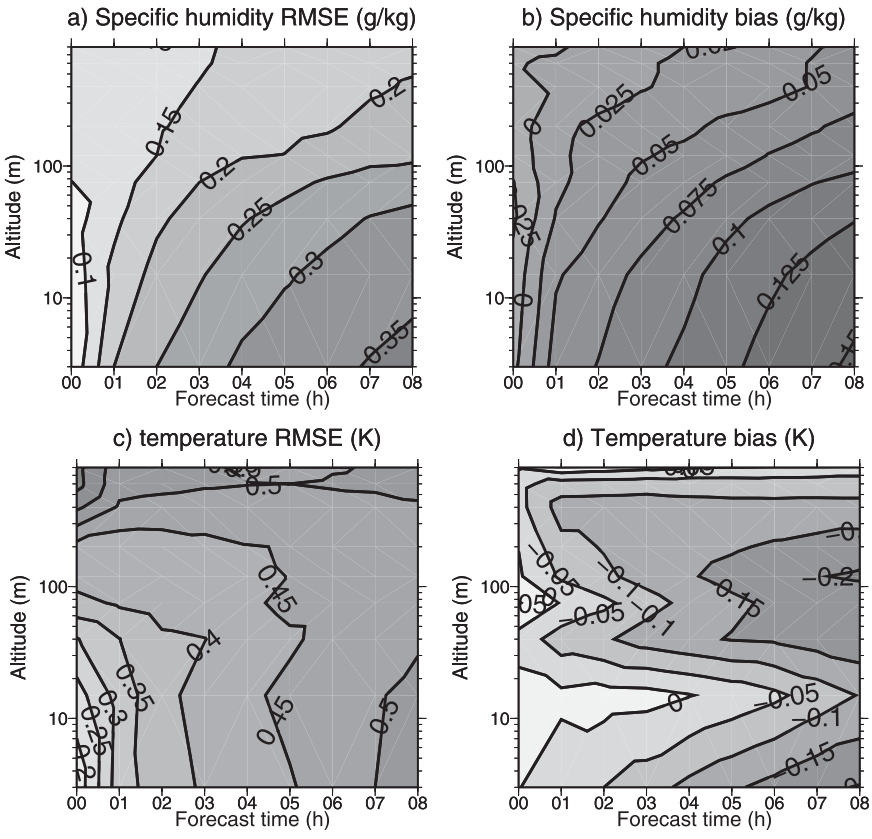

FIG. 2. (left) RMSE and (right) bias of (bottom) temperature and (top) specific humidity for NEAR-FOG. Isolines are every 0.05 K for temperature bias and RMSE every 0.05 g kg^{-1} for specific humidity RMSE, and every 0.025 g kg^{-1} for specific humidity bias.

1) THE NEAR-FOG SITUATION

Simulated observations corresponding to clear-sky and shallow-fog situations were produced. This observation set will be referred to as NEAR-FOG. Fifteen days of simulated observations were generated, during which no fog occurred for the first 10 nights. Shallow-fog situations developed for the remaining five nights. Their thicknesses did not exceed 10 m. Twenty-one hours of LVP conditions were ''observed'' for this situation. The skies above the model column were entirely clear, which ensured strong nighttime cooling. Figure 1 shows the ''true'' temperature at 1 m and corresponding liquid water path. Close to ground level, the daily highs lay in the 20°–22°C range, whereas the lows were around 8°–9°C. Day and night relative humidity varied greatly from 30% to 100%, corresponding to typical conditions observed during autumn and winter over land.

Figure 2 shows the mean root-mean-square error (RMSE) and the mean bias of the forecasted temperature and specific humidity versus forecast time and altitude when using the operational setup. The influence of the observations can be seen by the lower values of RMSE at initialization time below 50 m, especially for temperature. For temperature (Fig. 2c) and specific humidity (Fig. 2a), most of the increase of the RMSE occurred during the first 2 h of forecast time. For specific humidity, the maximum of RMSE is always at the surface, whereas for temperature the RMSE no longer showed large differences between the lower and upper part of the domain after 4 h of forecast time. The analysis is nearly unbiased for both specific humidity and temperature (Figs. 2b,d). The specific humidity bias became positive with forecast time, with a maximum close to the ground. A cold bias appeared rapidly for the forecasted temperature (Fig. 2d) and increased regularly with the forecast time, with maxima close to the ground level and above the top of the mast (30 m).

2) THE FOG SITUATION

This situation was designed to study the fog and low-cloud life cycle. Fog and low clouds occurred during many nights of the 15-day observation set referred to as FOG because of high moisture combined with strong nighttime cooling due to clear skies above the model

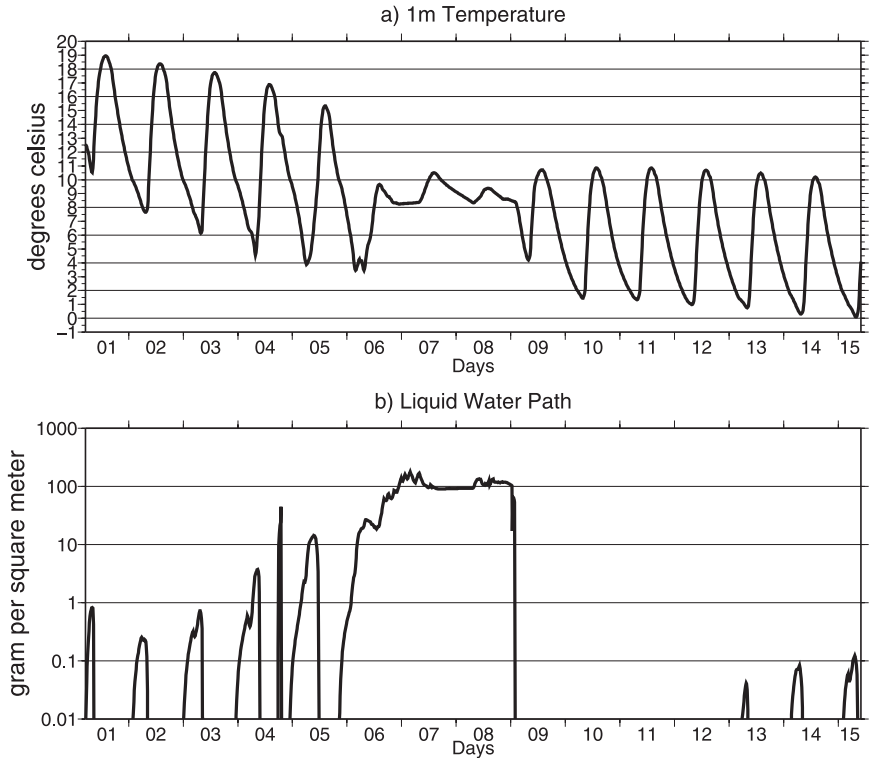

FIG. 3. As in Fig. 1, but for FOG.

column. Figure 3 shows the true temperature observations at 1 m and the true liquid water content integrated over the model column. In total, 98 h of LVP conditions were ''observed'' in these 15 days, with fog occurrence on 11 nights. Stratus also occurred in the upper part of the model column on days 7 and 8, which were not counted as LVP. Various fog situations occurred, from shallow early-morning fog to fog layers more than 200 m thick.

Figure 4 shows the mean RMSE and bias of temperature and specific humidity when using the operational setup with the FOG situation. It is interesting to compare it with Fig. 2. The initial profiles of specific humidity (Fig. 4a) show a larger RMSE for FOG than for NEAR-FOG over the whole domain. This is due to errors in the initialization of fog and low clouds. The increase of RMSE with forecast time is slower for FOG than for NEAR-FOG, and after 2 h of forecast, the values close to the surface are similar for both situations. The RMSE above 100 m remain significantly higher for FOG than for NEAR-FOG for all forecast times. The specific humidity bias (Fig. 4b) is close to zero for all forecasts time below 50 m, whereas it is negative above that height. For all heights, the specific humidity bias does not vary much with forecast time. The RMSE of forecasted temperature (Fig. 4c) increases much faster in the lower part of the domain for FOG than for NEAR-FOG (Fig. 2c) and reaches a maximum of 1 K after 7 h of simulation. A maximum appears between 50 and 150 m of altitude, which corresponds to situations where the forecasted height of the fog is different from the simulated observations. The inversion at the top of the fog layer significantly increases the error if the forecasted cloud layer thickness is not the same as the observed one. The temperature bias (Fig. 4d) also increases with forecast time, with a maximum at the surface.

3. Setup of the ensemble Kalman filter

a. Diagnosis of background error correlations

In the operational setup, the background error correlations were fixed in time and in the vertical direction. We diagnosed these correlations, using the National Meteorological Center (NMC) method (Parrish and Derber 1992). This method approximated the forecast error from a set of differences between several forecasts valid at the same time. Figure 5 presents the temperature and temperature-specific humidity correlations at analysis times of 0600 and 1500 UTC , averaged over the 1 November–31 January period. The error statistics follow a marked diurnal cycle, with higher values during the day corresponding to the development of a mixed boundary layer. The cross correlations between temperature and

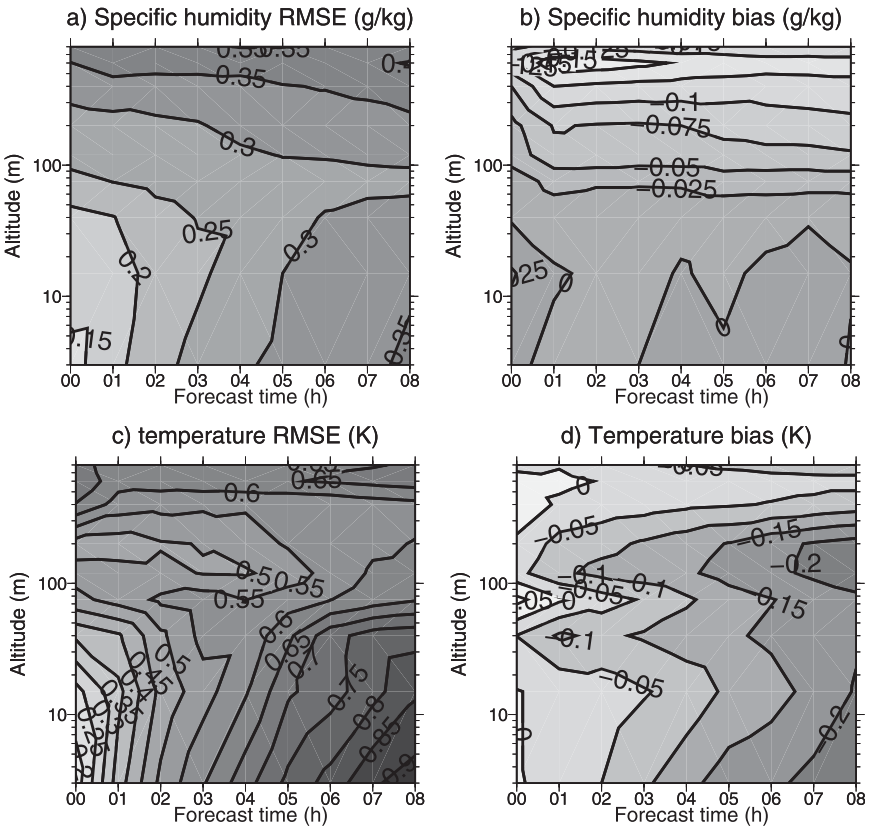

FIG. 4. As in Fig. 2, but for FOG.

specific humidity errors are higher during the night than during the day. At 0600 UTC and below 100 m, the cross correlations are nearly symmetric—that is, the correlation between the background temperature error at 10 m and humidity error at 50 m, for example, is close to the correlation between the background humidity and temperature errors at 10 and 50 m, respectively.

This analysis showed that we needed to build a more adaptive assimilation system that was able to estimate the flow-dependent background covariances for each run of the model and to take the cross correlations between temperature and humidity into account. The EnKF was a simple method to achieve that.

b. Construction of the ensemble

We implemented the ''perturbed observations'' configuration of the EnKF because it increases the spread of the ensemble as compared to other configurations. For more details on this, refer to Burgers et al. (1998). This version of the EnKF consists of using an ensemble of initial conditions that is built by adding white noise perturbations to the observations and mesoscale forcings.

In Eq. (1), for each ensemble member i the observation y_i^o is replaced by $y_i^o + \text{Normal}(0, \sigma_i^o)$. The observation error variances σ_i^o are known for the observations from the mast and the weather stations. As ALADIN profiles were also used as observations, their error statistics were estimated using a method proposed by Desroziers et al. (2005):

$$\sigma_o^2 = (\mathbf{H}\mathbf{x}^b - \mathbf{y}^o)(\mathbf{H}\mathbf{x}^a - \mathbf{y}^o). \tag{3}$$

Soil observations and mesoscale forcing (i.e., geostrophic wind, advection of temperature, and humidity) error statistics were provided by a sensitivity study carried out by Roquelaure and Bergot (2007).

The model has 30 levels for the two control variables of temperature and specific humidity (liquid water content is assimilated separately), which makes the dimensions of the model space in the assimilation scheme rather small, 60.

c. Validation of the prior ensemble

In this section, the realism of an ensemble of 32 backgrounds or priors is assessed. This assessment was carried out using rank histograms, also known as Talagrand histograms (Talagrand et al. 1997; Hamill 2001). It consists of ranking the verifying data in the sorted ensemble. Rank

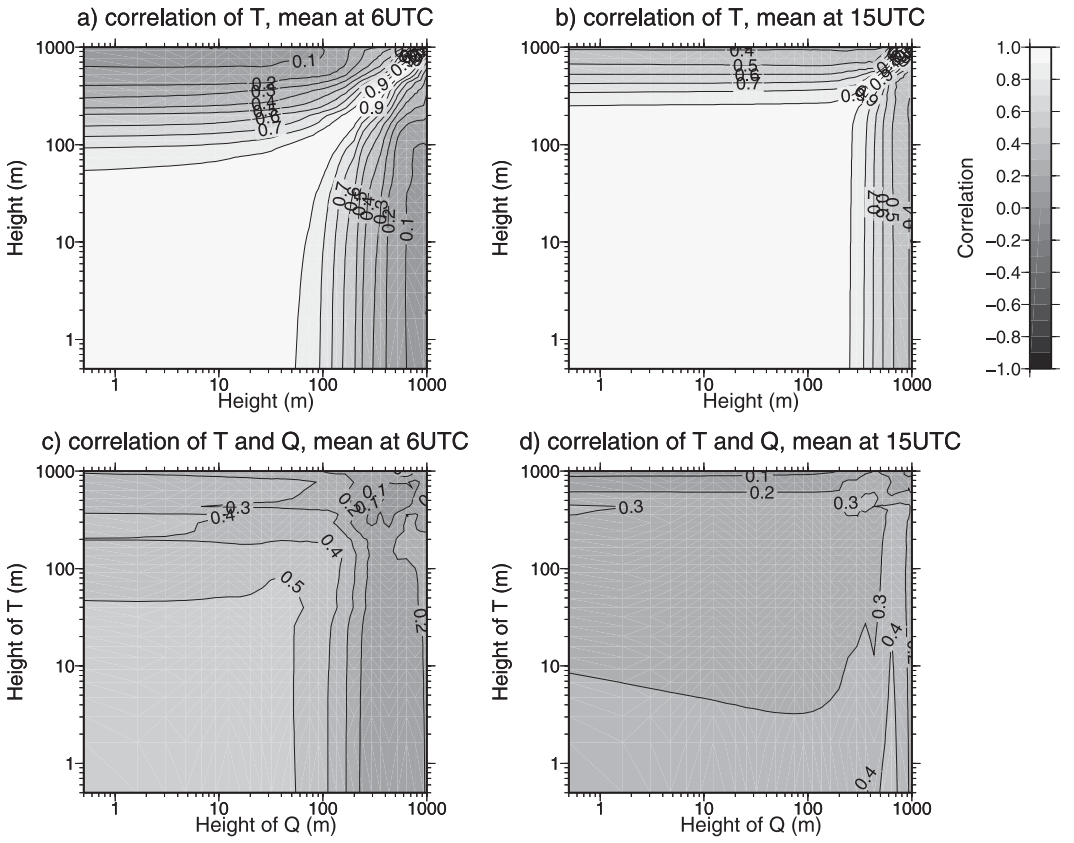

FIG. 5. Diagnosis of background correlations using the NMC method. Correlations of (top) temperature and of (bottom) temperature with specific humidity at (left) 0600 and (right) 1500 UTC over the 1 Nov 2005 to 31 Jan 2006 period.

histograms are generated by repeatedly comparing the rank of the verification (usually an observation) relative to values from an ensemble sorted from lowest to highest. They provide a rapid diagnosis of the ensemble reliability. A lack of variability in the ensemble will give a U-shaped rank histogram, whereas a convex shape indicates that the observations are most of the time encompassed in a subset of the actual ensemble, that is, that the ensemble spread is too large. Skewed histograms indicate a bias in the ensemble, that is, that the ensemble mean is biased. A flat shape implies equal probability of the verifying data and of the ensemble, hence that the ensemble is reliable. According to Hou et al. (2001), a rank histogram can be defined as flat if the adjusted missing rate is lower than 10%. To compute the adjusted missing rate, the missing rate, which is the sum of the relative frequencies of the two extreme (the first and the last) categories, is first computed. The adjusted missing rate is then defined as the difference between the expected missing rate $2/(N + 1)$ and the missing rate.

Figure 6 shows the rank histograms of the 32-member prior ensemble for temperature and humidity for the FOG and NEAR-FOG situations. The rank histograms were computed with two sets of verifying data: the simulated observations on the left and the truth on the right, to account for observation error. For both FOG and NEAR-FOG, the rank histogram was flat for temperature following the definition of Hou et al. (2001), which means that the ensemble was reliable for temperature. The missing rate (i.e., the sum of the relative frequency of the two extremes) is small according to the definition of Hou et al. (2001), which means that the spread of the ensemble was large enough (Figs. 6a,e). When observation error was taken into account (Figs. 6b,f), the convex shape of the rank histogram shows that the spread was even slightly too large. The small cold bias of the reference simulation (see Figs. 2 and 4) was reflected in the sloped rank histograms, which indicates that a majority of the ensemble members were generally too cold.

For specific humidity, the ensemble spread was insufficient by a greater amount for FOG than for NEAR-FOG (Figs. 6c,g). When observation error was taken into account (Figs. 6d,h), the rank histograms were flat,

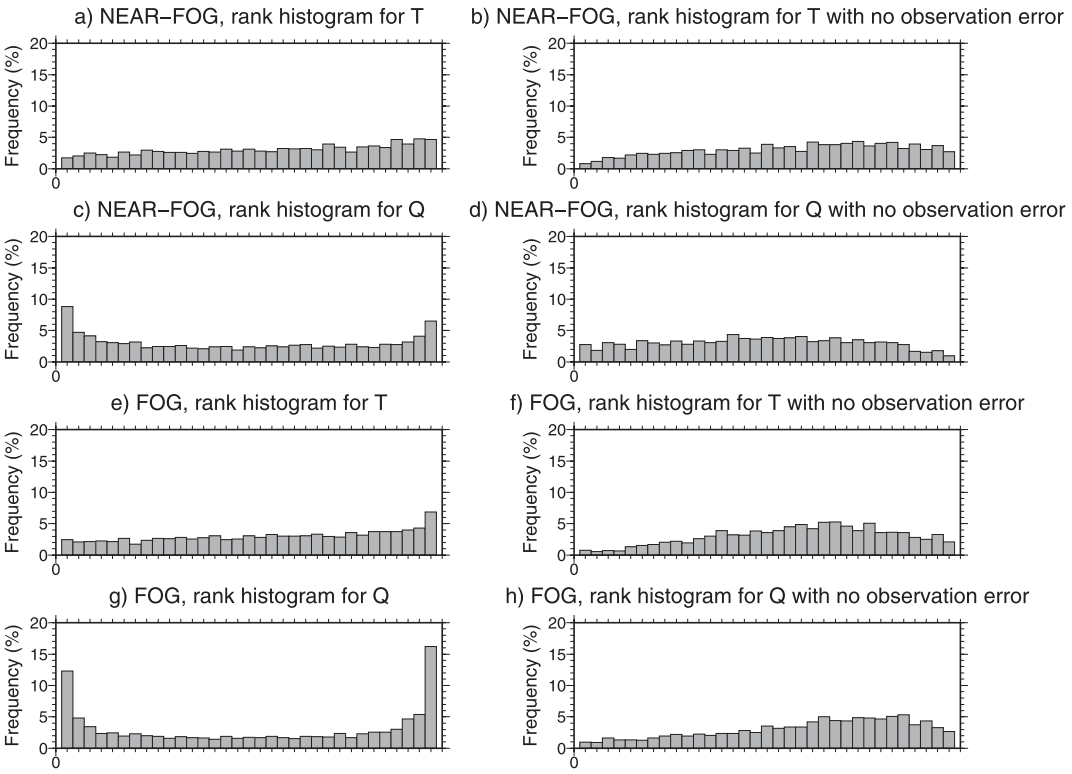

FIG. 6. Rank histograms for (a)–(d) NEAR-FOG and (e)–(h) FOG, of (a),(b),(e),(f) temperature and (c),(d),(g),(h) specific humidity. The *y* axis shows the frequency of the verifying observation; the *x* axis gives the bins formed by the ensemble. Verifying data are the simulated observations on the left; the truth on the right (i.e., observation error is accounted for in these rank histograms.

following the definitions of Hou et al. (2001). This means that the ensemble was fairly reliable, but that the observation error for specific humidity was too large, especially fog in the FOG situation. The positive (NEAR-FOG) and negative (FOG) specific humidity bias of the reference simulation (see Figs. 2 and 4) were reflected by the corresponding bias of the ensemble in both cases.

d. EnKF algorithm and its limitations

The EnKF is an adaptation of the Kalman filter (KF) model to nonlinear systems using Monte Carlo sampling (in the propagation step) and linear updating (correction or analysis step). In EnKF, an ensemble of backgrounds is integrated forward in time using the nonlinear forward model. A set of N analyses is thus propagated by the model into an ensemble of N backgrounds. At update times, the error covariance is calculated from the ensemble. The traditional BLUE update equation [Eq. (1)] is used to assimilate observations and build the initial conditions of temperature and humidity, with the Kalman gain calculated from the background error covariances [the $\mathbf{B}$ matrix of Eq. (1)] provided by the ensemble. At this stage, the ensemble of N backgrounds (or priors) is updated into N analyses (or posteriors). The ensemble allowed us to estimate the cross correlations of temperature and humidity errors in the background; the EnKF provided the possibility of building a multivariate assimilation scheme.

1) GAUSSIAN HYPOTHESIS

Although the EnKF does not require a linearization of the model, it is still based on the hypothesis that perturbations evolve linearly, so that initial Gaussian perturbations (i.e., perturbations completely represented by their mean and covariance) remain Gaussian within the assimilation time window. For a strongly nonlinear system, such as COBEL-ISBA, this assumption is generally not true. The variability of the measurement and state variables is small compared to their value, which means that the perturbations can be satisfactorily approximated to Gaussian. This constraint imposes a short (i.e., 1 h) assimilation cycle when the EnKF is used with COBEL-ISBA.

2) FILTER DIVERGENCE

The EnKF is often subject to filter divergence, that is, the distribution produced by the filter drifts away from the truth. Filter divergence normally occurs because the

prior probability distribution becomes too narrow (loss of ensemble spread) and the observations have progressively less impact on the model updates. This problem can be partly controlled by using a large ensemble; however, for practical field applications, the ensemble size needs to be kept relatively small for computational efficiency. Two methods for avoiding filter divergence are a configuration of the EnKF using a pair of ensembles (Houtekamer and Mitchell 1998; Houtekamer et al. 2005) and covariance inflation (Anderson and Anderson 1999; Anderson 2007, 2009); in this work, the latter method was chosen. Covariance inflation attempts to avoid filter divergence by simply inflating the covariance of the ensemble. Here, the adaptive covariance inflation of Anderson (2007) was applied. This algorithm adjusts the variance of the ensemble so that the observation falls within a reasonable distance, according to both ensemble variance and observation error variance, of the ensemble mean. It can be used only with observations with uncorrelated errors.

3) LOCALIZATION

The localization problem consists of spuriously large background covariance estimates between greatly distant grid points (Hamill et al. 2001). Such large covariances do not correspond to real correlations of errors between distant points; they are the results of noise in the estimate of covariances through an ensemble. This problem can be fixed by using a larger ensemble and by multiplying the **B**-matrix estimate element-wise by a correlation function with a compact support (Hamill et al. 2001); we used an exponential-based function, which was set to zero below a threshold level. The vertical length scale used was 200 m.

4. Ensemble Kalman filter assimilation of simulated observations

In this section, the simulations are evaluated against the true state of the atmosphere, generated by the reference run (REF). The EnKF was run with 32 members and the cross correlations of temperature and specific humidity were computed and used in the assimilation scheme. We used the multivariate configuration of the EnKF. In this study, this experiment will be referred to as ENKF32. For temperature and specific humidity scores, we will emphasize the results in the first 100 m of the model column, because this is the critical domain for the forecasting of radiation fog events.

The errors of the ALADIN profiles are uncorrelated between different levels within this framework. The covariance inflation factor was thus computed using the observations from the weather station, the mast, and the ALADIN profiles.

a. Results of the EnKF with NEAR-FOG

This EnKF was assessed in terms of temperature and specific humidity RMSE and bias for the NEAR-FOG situation. Figure 7 shows the RMSE of temperature and specific humidity with ENKF32, versus forecast time, as a percentage of the RMSE of the REF experiment. It also shows the bias difference between the two experiments for temperature and specific humidity. As the bias was of the same sign in both experiments, positive values indicate that ENKF32 was worse in terms of bias than REF.

For both temperature and specific humidity, the RMSE (Figs. 7a,c) of the initial conditions was improved by ENKF32. The improvement was larger above 50 m, which is the domain where there are no observations available. The background error variances computed by the ensemble were generally smaller than the ones used in the operational setup and also smaller than the estimated error variances of the ALADIN profiles. In consequence, the initial profiles were close to the background as compared to REF. The improvement of the scores above 50 m shows that, in the NEAR-FOG situation, the guess was closer to the real state of the atmosphere than the synthesized ALADIN profiles. As simulated observations are used, this result is not surprising because the true state of the atmosphere is also a forecast. The initial bias (Figs. 7b,d) was more or less unchanged below 100 m and showed a small degradation as compared with REF above that height.

After 1 h of forecast, the improvement of temperature RMSE by ENKF32 was much reduced and remained in the 5% range in the lower part of the domain until the end of the simulations. Above that height, the improvement was larger. The RMSE of forecasted specific humidity, on the other hand, was improved by 15%–20% below 50 m for all forecast times, and by 25%–35% above that height. The bias of forecasted specific humidity remained constant for all forecast times after a slight degradation in the first hour of simulation. The forecasted temperature bias also varied little after 1 h of forecast. It was slightly degraded below 30–50 m and above 300–400 m as compared to REF, and it lay in the same range as REF elsewhere.

Overall, the RMSE was improved slightly for specific humidity and considerably for temperature. The large improvement in initial conditions became smaller in the forecast, which shows the diminishing influence of initial conditions with longer forecast times. The temperature and specific humidity bias were both slightly degraded

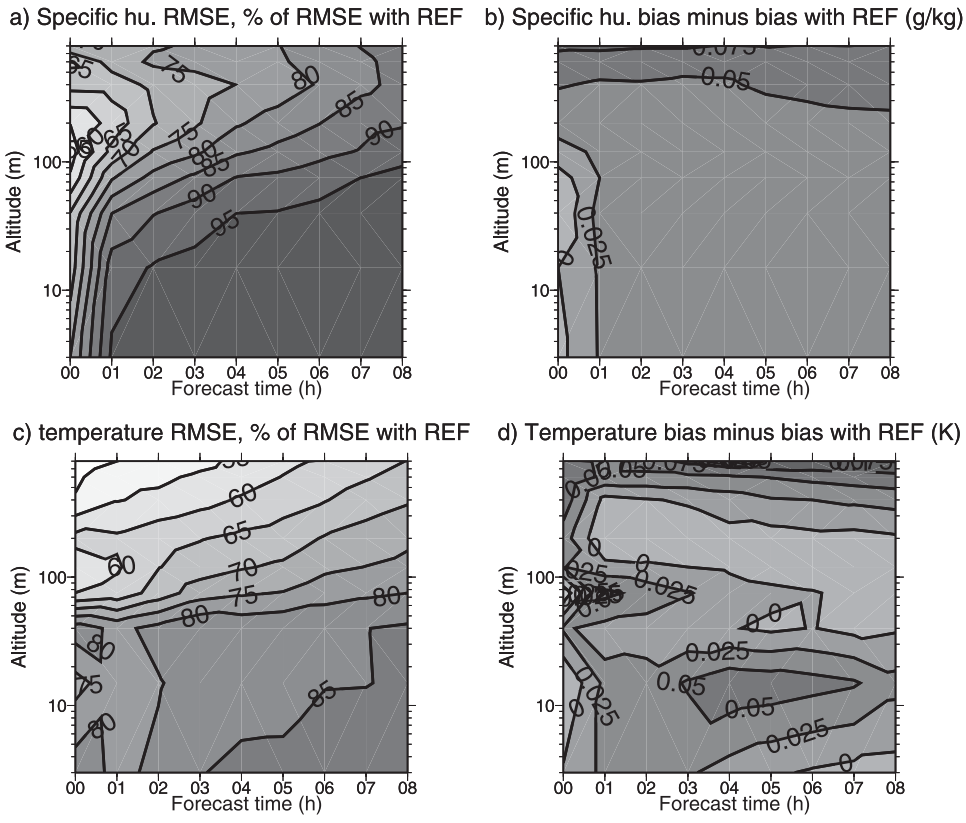

FIG. 7. (left) RMSE of ENKF32 as a percentage of the REF RMSE and (right) bias of (ENKF32 − REF) for (bottom) temperature and (top) specific humidity for NEAR-FOG.

by ENKF32 as compared with REF, which was also a consequence of being closer to the background in the initial conditions. The small model bias (see Fig. 2) was magnified in this case because the EnKF trusted the background more in the construction of the initial profiles, as compared to the operational setup.

b. Results of the EnKF with FOG

Here, the model was also assessed in terms of hit and false alarm ratios on the forecast of LVP conditions, in addition to scores of temperature and specific humidity. Scores for the onset and burn-off time of LVP conditions were also computed.

1) SCORES FOR TEMPERATURE AND SPECIFIC HUMIDITY

Figure 8 presents the RMSE and bias of temperature and specific humidity with ENKF32, as compared to those obtained with REF. It is interesting to compare the scores with Fig. 7 to see the impact of frequent fog on the performance of the EnKF. The RMSE of analyzed specific humidity and temperature (Figs. 8a,c) showed the same pattern between FOG and NEAR-FOG; a larger improvement as compared to REF above 100 m than below, and also a larger improvement for specific humidity than for temperature. The initial bias (Figs. 8b,d) was left mostly unchanged, except for the temperature bias above 600 m, which was slightly degraded.

The RMSE of forecasted specific humidity and temperature varied greatly between NEAR-FOG and FOG. Below 100 m, the initial improvement, as compared to REF diminished in the first 2 h of forecast and then increased to reach 30%–35% of improvement at the end of the simulations. The fact that the temperature and specific humidity RMSE's initial improvement persisted during the forecast was due to a better forecast of fog and low clouds thanks to better initial conditions (these results are illustrated in the next subsection). False alarms or nondetection of fogs had a strong impact on both temperature and specific humidity forecast error. The bias of forecasted specific humidity did not vary much with forecast time after 1 h of forecast. It was left unchanged below 50 m and slightly improved above, as compared to REF. The forecast temperature bias followed the same pattern as with NEAR-FOG. The degradation below 50 m and above 500 m was slightly larger with FOG.

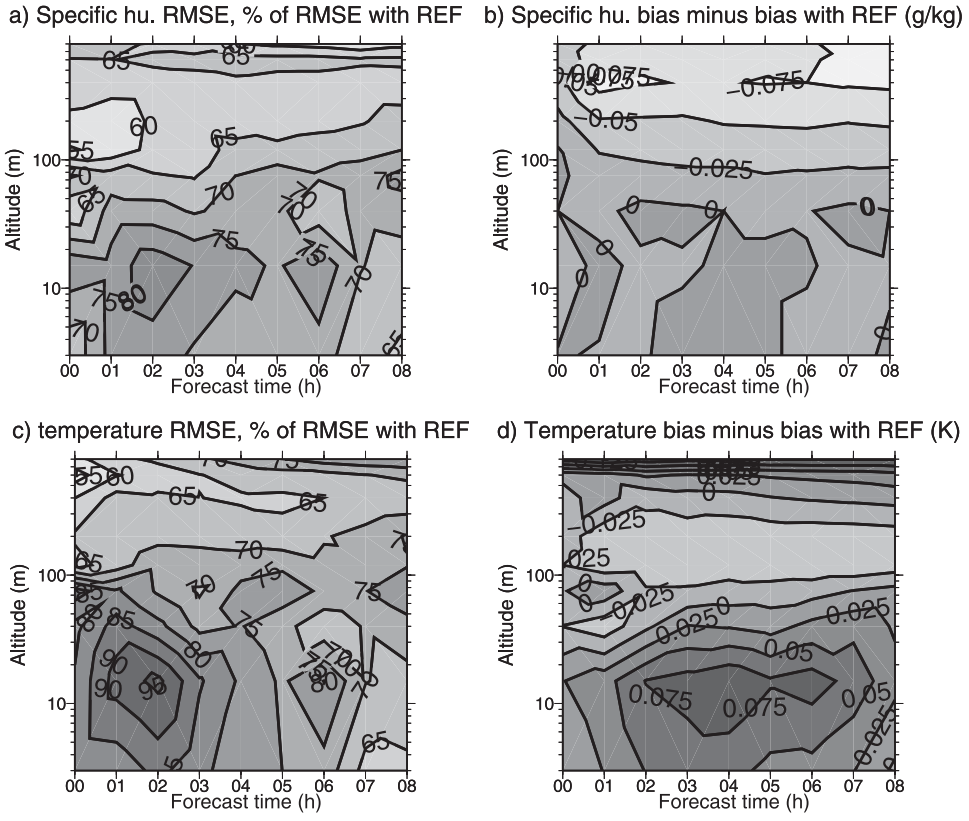

FIG. 8. As in Fig. 7, but for FOG.

2) FORECAST OF LVP CONDITIONS

Figure 9 shows the frequency distribution histogram of the onset and the burn-off time of LVP events, for all simulation times and forecast times, for the FOG situation. Simulations in which fog was already present at initialization time were discarded for the computation of the onset scores. For these simulations, it was meaningless to compare the simulated and observed onset times because the fog events considered had begun before the initialization time. The errors larger than 240 min are grouped together in the 240-min column.

For both REF and EnKF experiments, the forecast of the burn-off time was more accurate than that of the onset time. This is because the fogs that occurred between days 11 and 15 were shallow, they lifted very soon after sunrise, and the model forecasted these burn offs accurately. The REF experiment (Figs. 9a,c) showed a small early bias on the onset time. This was associated with the small cold bias noted in REF (see Fig. 4).

ENKF32 brought an improvement in the prediction of both the onset and burn-off times. The number of large errors was significantly reduced, and the number of simulations with errors smaller than or equal to 15 min was much increased. The bias on the forecast of onset time persisted, as the cold bias was not corrected by ENKF32.

Tables 1 and 2 show the hit ratio (HR) and pseudo–false alarm ratio (FAR) of LVP conditions for various forecast times and for the REF and ENKF32 experiments. In the case of rare event forecasting such as fog and LVP conditions, the pseudo-FAR is convenient because it removes the impact of the ''no-no good forecasts'' (no LVP forecast and no LVP observed), which mostly dominate the data sample and hide the true skill of the LVP forecast system. If a is the number of observed and forecasted events, b is the number of not observed and forecasted events, and c is the number of observed and not forecasted events, HR and pseudo-FAR are then defined as follows:

$$\mathrm{HR} = \frac{a}{a+c}; \quad \mathrm{pseudoFAR} = \frac{b}{a+b}.$$

Table 1 shows that the detection of LVP conditions was improved for all forecast times. The improvement was larger for longer forecast times, corresponding to the largest improvements in temperature and specific humidity RMSE as compared to REF. Also, the hit ratio of LVP conditions did not decrease with time with ENKF32, whereas it did with REF. This shows the strong influence

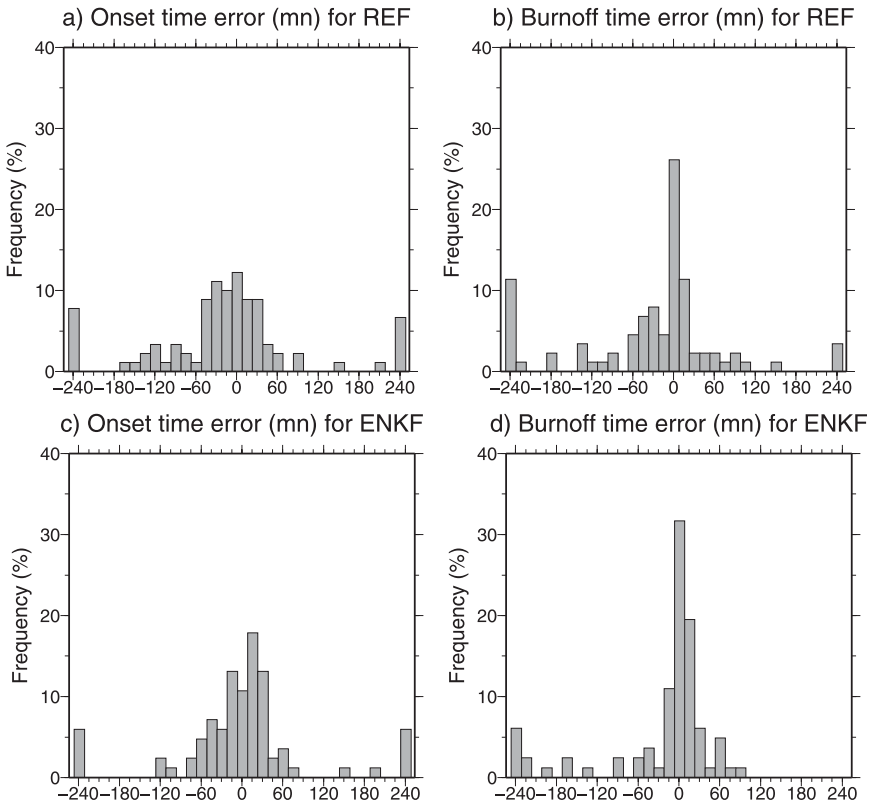

FIG. 9. (left) Frequency distribution histogram of the error on onset time (the LVP conditions at initial time are not taken into account) and (right) burn-off time of LVP conditions for the (top) REF experiment and (bottom) ENKF32 for FOG. Positive values correspond to a forecast of onset or burn off that is too late. Errors >240 min are grouped in the 240-min column.

of the initial conditions on the forecast when the model error has been removed by using simulated observations. Table 2 shows that ENKF32 experienced slightly fewer false alarms than REF. This is an interesting result because an improvement in both HR and FAR is hard to obtain.

c. *Impact of the EnKF on initial and forecasted lower boundary layer structure*

The situations we studied were characterized by swift and intense changes from one boundary layer stratification to another. This section will try to assess if the overall improvement brought by the ensemble Kalman filter on the scores was reflected in an improvement of the initial and forecasted stratification of the atmosphere. As mentioned before, this section will focus on the lower boundary layer, that is, the first 100 m of the COBEL-ISBA domain, where radiative fog occurs.

Figure 10 shows the initial and forecasted temperature profiles in the first 100 m of the COBEL-ISBA domain for REF and ENKF32, given by two simulations, one starting on day 6 at 0700 UTC and the other on day 3 at 1100 UTC. The real state of the atmosphere and the observations are also plotted. On day 6 at 0700 UTC, a 60-m-thick fog was present, which evolved to a 75-m-thick fog by 0900 UTC. The atmosphere was neutral within the fog, with a strong temperature inversion on top. On day 3 at 1100 and 1300 UTC, the sky was clear and the atmosphere was slightly unstable because of surface heating. The temperature analysis given by the

TABLE 1. HR of LVP conditions for various forecast times for the FOG situation and for the REF and ENKF32 experiments.

	1 h	2 h	3 h	4 h	6 h	8 h	All
REF	0.93	0.89	0.89	0.88	0.86	0.84	0.88
ENKF32	0.95	0.92	0.93	0.95	0.93	0.93	0.94

TABLE 2. Pseudo-FAR of LVP conditions for various forecast times for the FOG situation and for the REF and ENKF32 experiments.

	1 h	2 h	3 h	4 h	6 h	8 h	All
REF	0.07	0.05	0.07	0.10	0.12	0.18	0.09
ENKF32	0.04	0.03	0.02	0.06	0.08	0.15	0.07

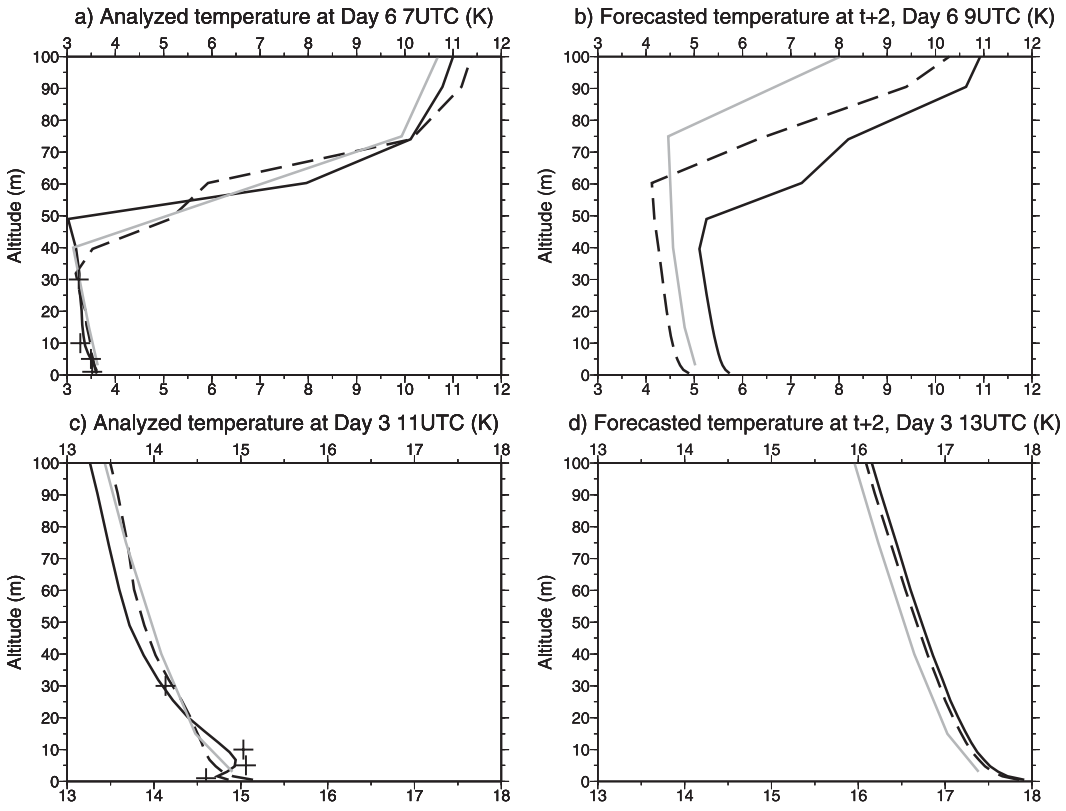

FIG. 10. FOG temperature profiles of (a),(c) temperature at initialization time and (b),(d) temperature after 2 h of simulation for simulations starting on (top) day 6 at 0700 UTC and (bottom) day 3 at 1100 UTC. REF is plotted by the black continuous line, ENKF32 by the dashed line, and the truth by the gray line. Observations at analysis time are plotted by black crosses.

EnKF is closer to the real state of the atmosphere for the two considered cases. REF was more influenced by the observations than ENKF32. As a consequence, the operational setup produced a stable initial temperature profile while the atmosphere was slightly unstable, whereas ENKF32 gave a slightly unstable initial temperature profile. This improvement in the initial stratification of the lower boundary layer led to a better forecast. After 2 h of forecast, there were not much difference in the stratification as forecasted by REF and ENKF32; however, the latter was closer to the real state of the atmosphere in both cases.

As illustrated by these two examples, ENKF32 provided initial profiles that were generally closer to the true stratification of the atmosphere than REF. This is probably the reason why the forecasts of temperature, specific humidity, and fog events were also improved by ENKF32 as compared to REF.

d. Impact of the cross correlations of temperature and humidity errors in the background

In the ENKF32 experiment, the cross correlations of temperature and specific humidity in the background were taken into account. To assess the impact of these cross correlations on the quality of the initial conditions, an experiment called ENKF32_MONO was run without taking these cross correlations into account; this experiment was run with a monovariate configuration of the EnKF. Figure 11 shows the temperature RMSE mean over all simulations of ENKF32_MONO as a percentage of the temperature RMSE of ENKF32 versus forecast time for FOG and NEAR-FOG. The scores were not shown for specific humidity as they were mostly similar. For NEAR-FOG, the impact of the cross correlations was slightly negative for temperature RMSE and slightly positive for specific humidity RMSE. For FOG, the impact was significantly positive for both temperature and specific humidity RMSE, especially for forecast times larger than 3 h and below 100 m. For NEAR-FOG and FOG, the bias on forecasted temperature and specific humidity was not changed much by the multivariate configuration of the EnKF. Overall, the multivariate EnKF brought small changes for the NEAR-FOG situation and an improvement for the FOG situation, as compared to the monovariate EnKF. For FOG, the quality of the fog forecasts (not shown)

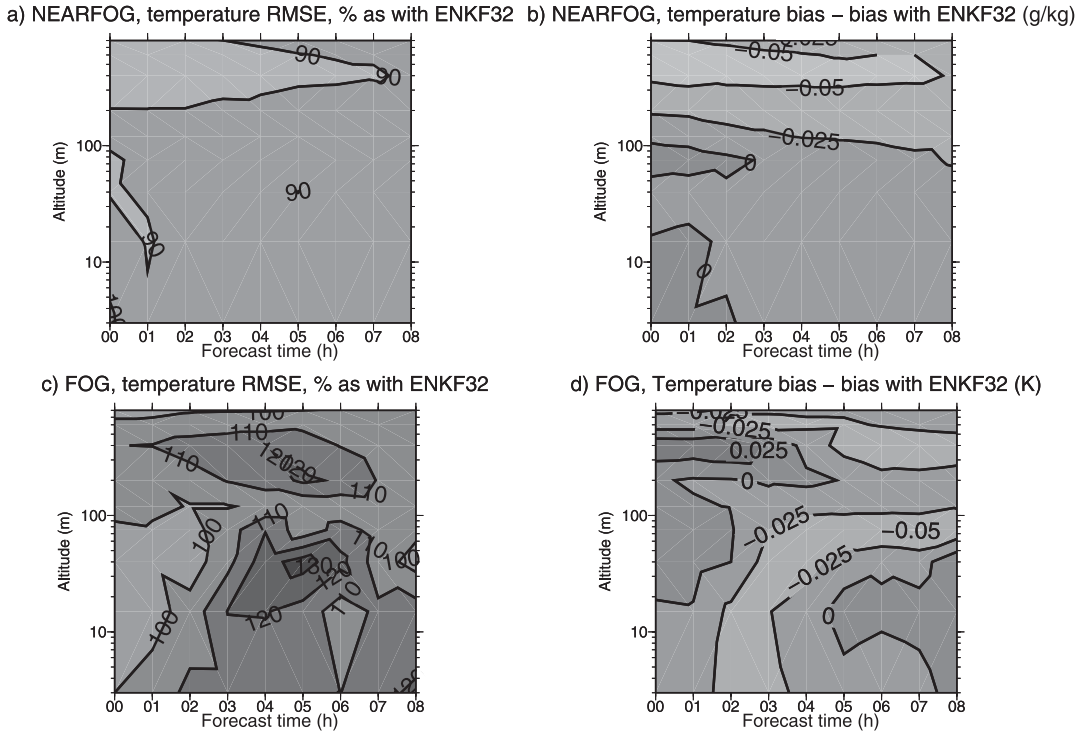

FIG. 11. Temperature of ENKF32_MONO RMSE as (left) a percentage of the ENKF32 RMSE and (right) bias of ENKF32_MONO − ENKF32 vs forecast time for (top) NEAR-FOG and (bottom) FOG.

was also improved by the multivariate configuration of the EnKF as compared to the monovariate configuration. The different behavior between NEAR-FOG and FOG was due to the fact that cross correlations were on average larger for FOG than for NEAR-FOG.

To explain why the cross correlations were higher on average for FOG than for NEAR-FOG, Fig. 12 shows the temperature and temperature-specific humidity correlations as computed by the 32-member ensemble for two simulations: one starting on day 4 at 1200 UTC and the other starting on day 6 at 0700 UTC. These correlations were the ones used in the assimilation scheme to compute the initial profiles of temperature and specific humidity. On day 4 at 1200 UTC, the skies were clear whereas on day 6 at 0700 UTC, 50-m-thick fog was present at initialization time. Areas of high temperature correlations (Figs. 12a,b) correspond to the mixed layer. Its height varied considerably between day and night. On day 6 at 0700 UTC, the top of the mixed layer matched the top of the fog layer and the correlations were very small above that height. On day 4 at 1200 UTC, the top of the mixed layer lay at around 150 m. The cross correlations differed a lot between the two dates. On day 6 at 0700 UTC, they were very high in the cloud layer (i.e., below 50 m). This is because in a saturated environment the specific humidity equals the saturated specific humidity, which depends on temperature. An error in temperature automatically leads to an error in specific humidity in these conditions. Strong negative cross correlations occurred between humidity above the cloud layer and temperature inside the cloud layer, with values ranging from −0.6 to −0.8. These cross correlations were not symmetric, there were no correlations between temperature above the fog and specific humidity below. The cross correlations were much lower on day 4 at 1200 UTC, whether they were positive (in the mixed layer) or negative (above the boundary layer for temperature). Because the occurrence of saturated conditions is much more frequent during FOG than during NEAR-FOG, the average cross correlations are also larger on average.

5. Ensemble Kalman filter assimilation of real observations

In this section, experiments are reported that used real observations from Charles de Gaulle Airport, over the winter of 2004/05. For this situation, the reference experiment was called REAL. The EnKF was run with 8, 16, and 32 members and the cross correlation of temperature and specific humidity errors was taken into account. As for other situations, the experiments were

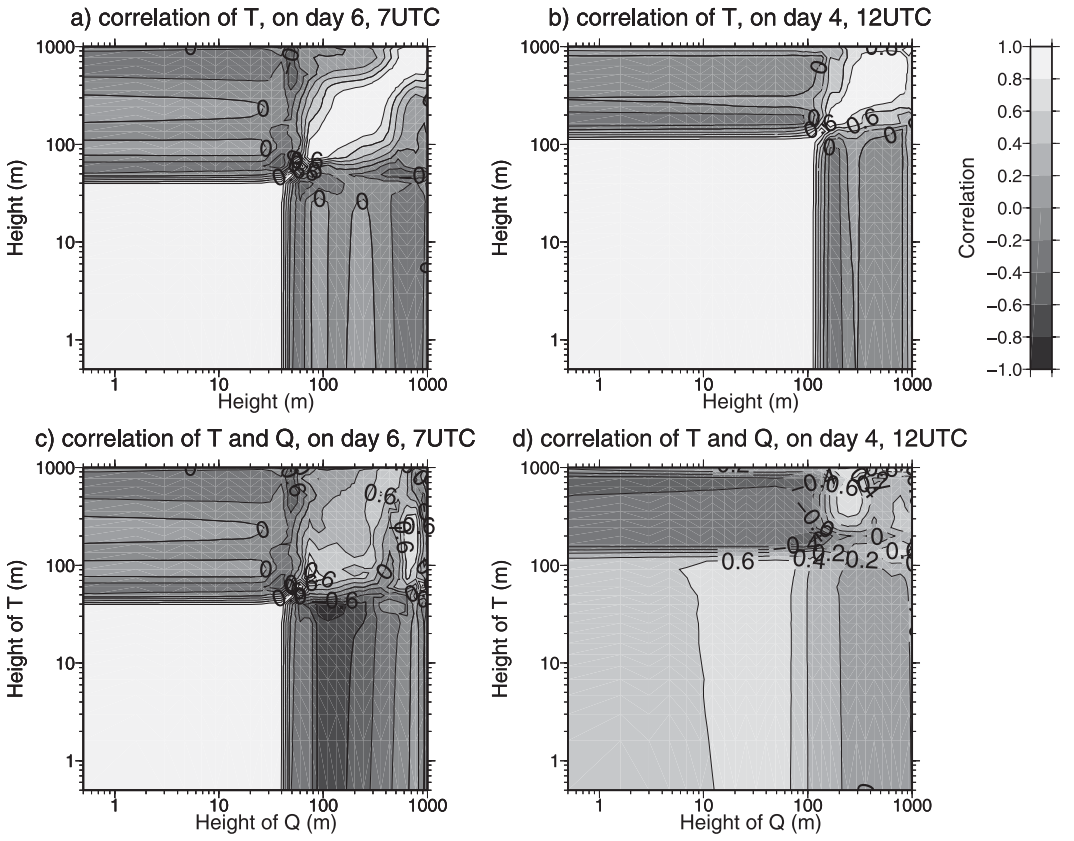

FIG. 12. Background error correlations in the as computed by the 32-member ensemble for FOG of (top) temperature and (bottom) temperature with specific humidity on day (left) 6 at 0700 UTC and (right) day 4 at 1200 UTC.

called ENKF8, 16, and 32. This section focuses on ENKF32; the impact of the ensemble size will be discussed in the next section. When using real observations, the ALADIN errors are not correlated between different levels; this means that we cannot use the ALADIN profiles in the computation of the covariance inflation factor.

The test period covered November and December 2004 and January 2005, with hourly assimilation simulation cycles, representing around 2200 eight-hour simulations. Here, 186 h of LVP conditions were observed during these months. Fog and low-cloud conditions were more frequent late at night and early in the morning and were less frequent during the afternoons. Observations were available only for heights ranging from 1 to 30 m, so when using real observations, the impact of the EnKF on the model was assessed only in terms of the quality of LVP condition forecasts.

a. LVP conditions forecast

Tables 3 and 4 display the mean HR and pseudo-FAR of LVP conditions for various forecast times for the REAL case.

Both HR and pseudo-FAR were slightly improved by ENKF32 as compared to REAL for forecast times between 1 and 3 h. Beyond that, there was not much change. This shows that the initial conditions had a smaller impact on the quality of the fog forecasts when real observations were used compared to when simulated observations were used. The influence of errors in both the model and the mesoscale forcings was larger than the influence of initial conditions beyond the first 3 h of forecast time. This matches the conclusions of Roquelaure and Bergot (2007), who showed that errors on the initial conditions have more impact for forecast times smaller than 3 h, and that errors on mesoscale forcings have more impact for larger forecast times.

b. Onset and burn off of LVP events

Tables 5 and 6 show the error of the predicted time of onset and burn off for all simulation and forecast times. Simulations in which fog was present at initialization were discarded when computing the score for fog onset, for the same reasons as mentioned before.

ENKF32 brought a small improvement as compared to REAL for the forecast of the LVP onset time. There

TABLE 3. HR of LVP conditions for various forecast times for the REAL situation and for the REF, ENKF8, ENKF16, and ENKF32 experiments.

	1 h	2 h	3 h	4 h	6 h	8 h	All
REF	0.78	0.62	0.64	0.61	0.59	0.52	0.63
ENKF8	0.73	0.60	0.59	0.54	0.55	0.52	0.60
ENKF16	0.75	0.64	0.67	0.60	0.58	0.50	0.63
ENKF32	0.78	0.66	0.70	0.61	0.59	0.52	0.64

were around 10% more cases of small errors (between 0 and 90 min) and 10% fewer with errors larger than 360 min. On the other hand, ENKF32 did not improve the forecast of burn-off times much. The EnKF had less impact on the forecast of fog burn-off times because for most of the cases fog was already present at initialization time. For these cases, the burn-off time depended mainly on the initial thickness of the fog layer and on the forecasted soil temperature and water content. Their values were weakly correlated with initial profiles of temperature and humidity.

6. Impact of the ensemble size

In all previous experiments, the EnKF was run with a 32-member ensemble. Here, the EnKF was run with smaller ensembles, 8 members (experiment ENKF8) and 16 members (ENKF16). The consequence of smaller ensembles is a smaller spread and a poorer description of the variance–covariance matrix by the ensemble. For this reason, smaller ensembles increase the risk of filter divergence.

a. Simulated observations

Figure 13 shows the RMSE of the initial profiles of temperature and specific humidity for ENKF8 and ENKF16 for all simulations as a percentage of the RMSEs obtained with ENKF32 for FOG and NEAR-FOG. For NEAR-FOG, the size of the ensemble had a mostly positive impact on the RMSE of initial specific humidity and a mostly negative one on temperature. For FOG, a larger ensemble brought no improvement. For both FOG and NEAR-FOG, the size of the ensemble had a more positive impact on specific humidity than on temperature. This can be explained by the characteristics of the ensemble. For temperature, the spread of 8-, 16-, and 32-member ensembles was large enough. In this case, adding new members did not bring much more information on the error statistics. For specific humidity, the ensemble spread was slightly insufficient, smaller for ENKF8 than for ENKF16 and smaller for ENKF16 than for ENKF32. In this case, adding new members was useful.

TABLE 4. Pseudo-FAR of LVP conditions for various forecast times for the REAL situation and for the REF, ENKF8, ENKF16, and ENKF32 experiments.

	1 h	2 h	3 h	4 h	6 h	8 h	All
REF	0.25	0.41	0.48	0.47	0.48	0.53	0.46
ENKF8	0.28	0.42	0.50	0.50	0.51	0.50	0.46
ENKF16	0.26	0.40	0.46	0.48	0.50	0.51	0.46
ENKF32	0.23	0.38	0.43	0.48	0.50	0.53	0.45

TABLE 5. Number of simulations falling into the error intervals (min) for the prediction of the onset of fog events during REAL.

	No.	No.	No.	No.	No.	No.	No.
REF	28	26	22	28	16	18	68
ENKF32	30	28	24	28	12	22	62

Overall, increasing the size of the ensemble did not greatly improve the initial conditions. This is because the adaptive covariance inflation algorithm compensated for the smaller spreads caused by smaller ensembles. Figure 14 shows the mean covariance inflation factor for temperature and specific humidity versus simulation time, for NEAR-FOG (Figs. 14a,b) and FOG (Figs. 14c,d). For both situations, the covariance inflation factors were larger for ENKF8 than for ENKF16 and also larger for ENKF16 than for ENKF32. A smaller spread of the ensemble resulted in larger covariance inflation. For temperature (Figs. 14a,c), the covariance inflation factor followed a strong diurnal cycle for NEAR-FOG and a slightly less marked one for FOG. This diurnal cycle corresponded to a diurnal cycle of the temperature covariances. During the day, the differences among the N analyses were greater than among the N backgrounds, as the forward integration by the model erased the perturbations to produce neutral or unstable stratified profiles. In contrast, during the night the atmosphere was stable and the perturbations of the analysis were better preserved by the forward integration in this case. In consequence, the spread of the ensemble of N backgrounds was larger for temperature during the night than during the day, and the covariance inflation compensated for this with larger values during the day. This phenomenon was less marked for FOG than for NEAR-FOG, because the atmosphere was less often unstable during the day and less often stable during the night because of the more frequent occurrence of fog.

TABLE 6. As in Table 5, but for the prediction of burn-off time.

Min	0–5	15–45	45–90	90–180	180–240	240–360	>360
REF (No.)	48	28	26	24	10	10	32
ENKF32 (No.)	50	16	20	44	8	4	38

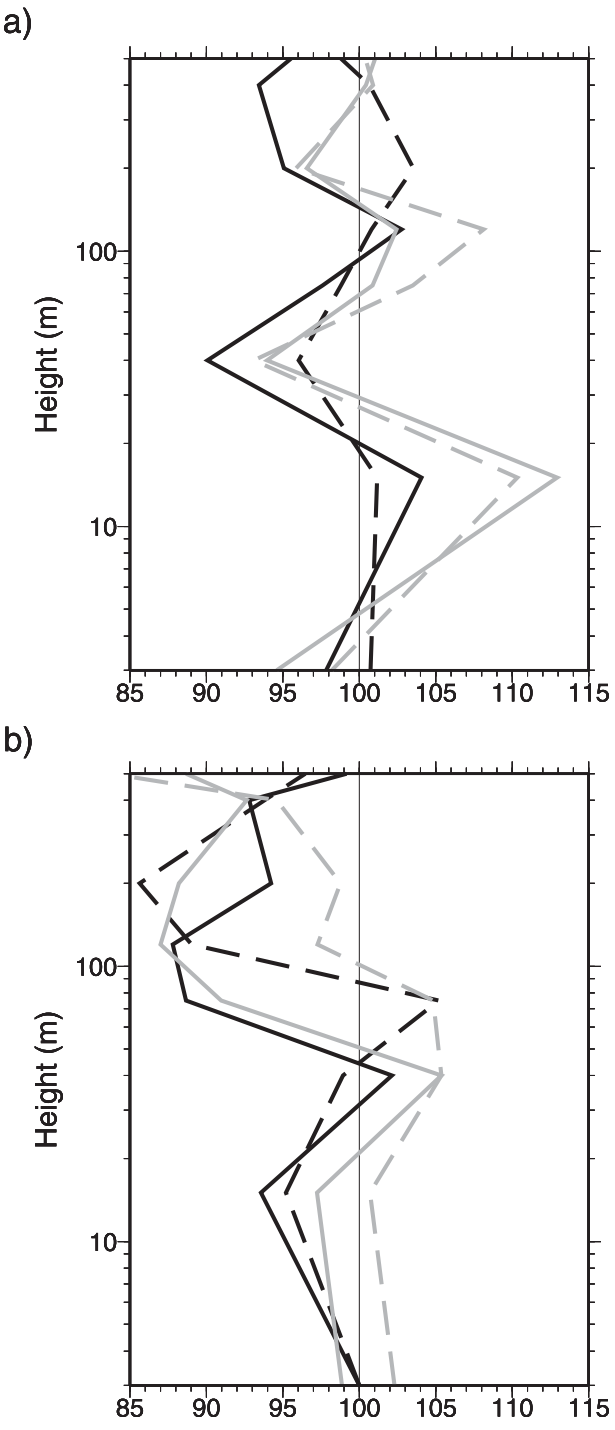

FIG. 13. RMSE of initial temperature (black) and specific humidity (gray) of ENKF8 (continuous line) and of ENKF16 (dashed line) as a percentage of the ENKF32 RMSE for (a) NEAR-FOG and (b) FOG.

The specific humidity covariance inflation factor (Figs. 14b,d) had much higher values for NEAR-FOG as compared to FOG. This was probably due to the higher frequency of saturated profiles in the prior ensemble and in the observations. When profiles are saturated, the simulated observations and the ensemble mean are very close, which removes the need for covariance inflation. The high values of the specific covariance inflation factor for NEAR-FOG were linked to the smaller spread mentioned before (see Fig. 6c). This shows that the adaptive covariance algorithm is an indispensable and efficient tool for preventing filter divergence. It allows runs with rather small-sized ensembles when using simulated observations.

b. Real observations

Tables 3 and 4 show HR and pseudo-FAR of LVP conditions versus forecast time for ENKF8, ENKF16, and ENKF32 in the REAL situation. For both HR and FAR, the size of the ensemble had a significant impact on the scores. The impact was smaller for forecast times longer than 4 h. This shows that the ensemble size matters more with real observations than with simulated observations, especially for the first few hours of the forecast. The covariance inflation (Figs. 14e,f) was small for temperature and very small for specific humidity. It could be because the covariance inflation factor was computed without using the ALADIN profiles when using real observations. Because of model error, more members were needed to build a reliable ensemble and covariance inflation seemed to be less efficient when using real observations. A larger ensemble is needed when real observations were used, as compared to simulations using simulated observations.

7. Summary and discussion

Fog is a physical phenomenon that remains particularly difficult to forecast. To render a 1D approach useful, local observations have to be used to provide accurate initial profiles. A simple diagnosis showed that the error correlations of the background depended on the stability of the atmosphere. Also, this study showed that correlations between temperature and specific humidity errors in the background could not be ignored. These insights led to the implementation of an ensemble Kalman filter, which allowed it to dynamically estimate the background error statistics. With simulated observations, the EnKF brought a marked improvement in the initial and forecasted temperature and specific humidity. It also greatly improved the quality of the forecast of fog events, in terms of hit ratio and pseudo–false alarm rates. It increased the accuracy in forecasting the

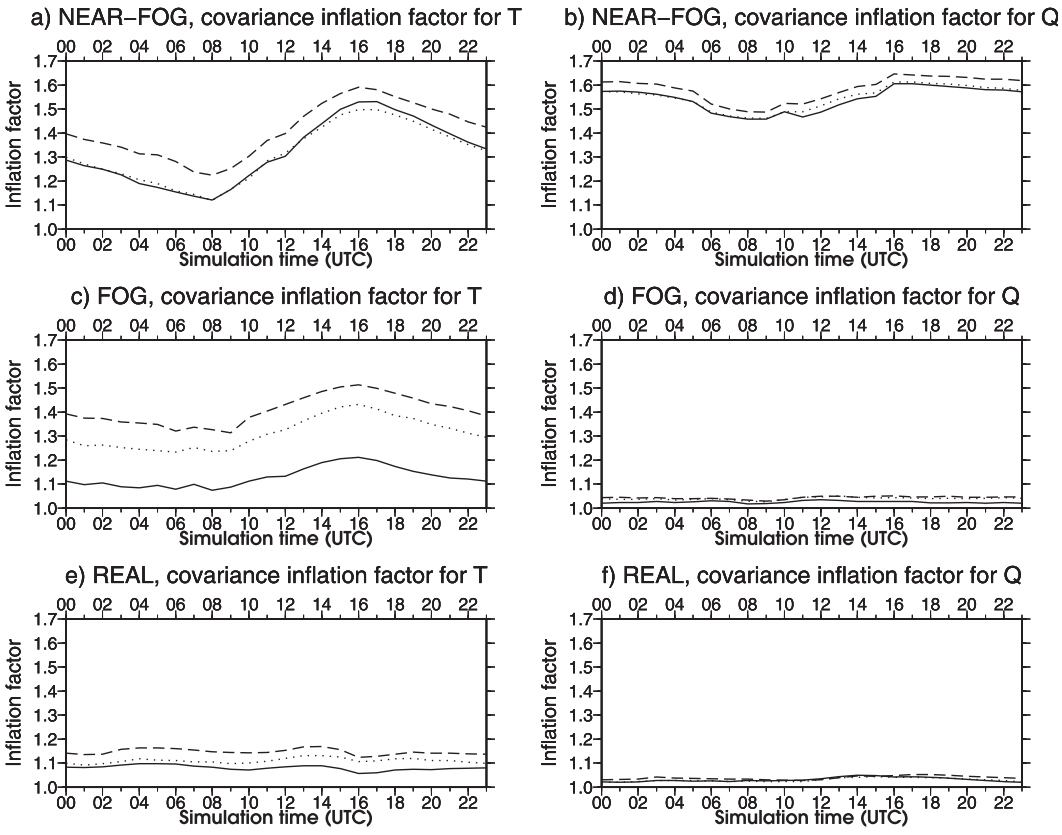

FIG. 14. (left) Mean temperature and (right) specific humidity covariance inflation factor vs simulation time for (a),(b) NEAR-FOG, (c),(d) FOG, and (e),(f) REAL. Covariance inflation factors computed for ENKF8 are plotted as a dashed line, for ENKF16 as a dotted line, and for ENKF32 as a continuous line.

onset and burn-off times of LVP conditions, which is the result that matters most to the airports. The impact of cross correlations was shown to be mostly positive.

Simulated observations constitute a very different framework from real observations. The fact that the model error was avoided with simulated observation allowed a better understanding of the sources of error at initialization and of the relations between the initial and the forecast profiles. Using real observations, the EnKF brought an improvement in the forecast of fog for forecast times shorter than 3 h. The scores were left unchanged for larger forecast hours. The forecast of the onset time of LVP conditions was also improved. The scores on the burn-off time were not, but the fact that liquid water was often present at initialization time for these simulations hid the impact of the EnKF. When real observations were used, the model and mesoscale-forcing errors were added to the initial condition errors, also present with simulated observations, so that the influence of the initial condition errors on the forecast was relatively smaller in that case. Furthermore, model errors are not taken into account in the version of the BLUE algorithm that was used. They are notably hard to estimate. A possible method is to build a multischeme ensemble, using different physical parameterizations (e.g., turbulence, microphysics, and radiation scheme). Overall, despite this limitation, which is intrinsic to the model, the EnKF is an interesting assimilation scheme for the forecasting of radiation fog events.

The ensemble size was more correlated to the quality of the initial conditions and forecasts with real observations than with simulated observations. With simulated observations, the covariance inflation algorithm managed to compensate for the lack of spread of smaller ensembles and allowed us to run the EnKF with satisfactory results with an ensemble of only eight members. When using real observations, a larger ensemble is needed. The EnKF works well within a 1D approach with relatively few members, which renders its use possible in an operational context.

Several studies have shown that for strongly nonlinear systems such as a 1D model, an alternative to variational and Kalman filtering methods exists: the particle filter. This assimilation scheme does not need any Gaussian

assumption and has been shown to work well with theoretical chaotic systems such as the Lorenz system. Work is ongoing on this promising method.

Acknowledgments. We wish to thank the editors and the anonymous reviewers for their valuable comments and suggestions, which improved the manuscript. We are also grateful to Robert Tardif and Gérald Desroziers for their comments.

REFERENCES

Anderson, L., 2007: An adaptive covariance inflation error correction algorithm for ensemble filters. *Tellus,* **59,** 210–224.

——, 2009: Spatially and temporally varying adaptive covariance inflation for ensemble filters. *Tellus,* **61A,** 72–83.

——, and S. Anderson, 1999: A Monte Carlo implementation of the nonlinear filtering problem to produce ensemble assimilations and forecasts. *Mon. Wea. Rev.,* **127,** 2741–2758.

Bergot, T., 1993: Modélisation du brouillard à l'aide d'un modèle 1d forcé par des champs mésoéchelle: Application à la prévision. Ph.D. thesis, Université Paul Sabatier, 192 pp.

——, and D. Guédalia, 1994a: Numerical forecasting of radiation fog. Part I: Numerical model and sensitivity tests. *Mon. Wea. Rev.,* **122,** 1218–1230.

——, and ——, 1994b: Numerical forecasting of radiation fog. Part II: A comparison of model simulation with several observed fog events. *Mon. Wea. Rev.,* **122,** 1231–1246.

——, D. Carrer, J. Noilhan, and P. Bougeault, 2005: Improved site-specific numerical prediction of fog and low clouds: A feasibility study. *Wea. Forecasting,* **20,** 627–646.

Boone, A., 2000: Modélisation des processus hydrologiques dans le schéma de surface isba: Inclusion d'un réservoir hydrologique, du gel et modélisation de la neige. Ph.D. thesis, Université Paul Sabatier, 207 pp.

Bougeault, P., and P. Lacarrere, 1989: Parameterization of orography-induced turbulence in a mesoscale model. *Mon. Wea. Rev.,* **117,** 1872–1890.

Burgers, G., P. V. Leuwen, and G. Evensen, 1998: Analysis scheme in the ensemble Kalman filter. *Mon. Wea. Rev.,* **126,** 1719–1724.

Clark, D., 2002: The 2001 demonstration of automated cloud forecast guidance products for San Francisco International Airport. Preprints, *10th Conf. on Aviation, Range, and Aerospace Meteorology,* Portland, OR, Amer. Meteor. Soc., JP1.26. [Available online at http://ams.confex.com/ams/13ac10av/techprogram/paper_38862.htm.]

——, 2006: Terminal ceiling and visibility product development for northeast airports. Preprints, *12th Conf. on Aviation, Range, and Aerospace Meteorology,* Atlanta, GA, Amer. Meteor. Soc., P1.15. [Available online at http://ams.confex.com/ams/Annual2006/techprogram/paper_103710.htm.]

Desroziers, G., L. Berre, B. Chapnik, and P. Poli, 2005: Diagnosis of observation, background and analysis-error statistics in observation space. *Quart. J. Roy. Meteor. Soc.,* **131,** 3385–3396.

Estournel, C., 1988: Etude de la phase nocturne de la couche limite atmospherique. Ph.D. thesis, Université Paul Sabatier, 161 pp.

Evensen, G., 1994: Sequential data assimilation with a nonlinear quasi-geostrophic model using Monte Carlo methods to forecast error statistics. *J. Geophys. Res.,* **99,** 10 142–10 162.

——, 2003: The ensemble Kalman filter: Theoretical formulation and practical implementation. *Ocean Dyn.,* **53,** 343–367.

Hacker, J., and C. Snyder, 2005: Ensemble kalman filter assimilation of fixed screen-height observations in a parametrized PBL. *Mon. Wea. Rev.,* **133,** 3260–3275.

——, and D. Rostkier-Edelstein, 2007: PBL state estimation with surface observations, a column model, and an ensemble filter. *Mon. Wea. Rev.,* **135,** 2958–2972.

Hamill, M., 2001: Interpretation of rank histograms for verifying ensemble forecasts. *Mon. Wea. Rev.,* **129,** 550–560.

——, J. Whitaker, and C. Snyder, 2001: Distance-dependant filtering of background error covariance estimates in an ensemble Kalman filter. *Mon. Wea. Rev.,* **129,** 2776–2790.

Herzegh, P., S. Benjamin, R. Rasmussen, T. Tsui, G. Wiener, and P. Zwack, 2003: Development of automated analysis and forecast products for adverse ceiling and visibility conditions. Preprints, *19th Int. Conf. on Interactive Information and Processing Systems for Meteorology, Oceanography, and Hydrology,* Long Beach, CA, Amer. Meteor. Soc., 9.3. [Available online at http://ams.confex.com/ams/pdfpapers/57911.pdf.]

Hou, D., E. Kalnay, and K. Droegemeier, 2001: Objective verification of the SAMEX '98 ensemble forecasts. *Mon. Wea. Rev.,* **129,** 73–91.

Houtekamer, P., and H. Mitchell, 1998: Data assimilation using an ensemble Kalman filter technique. *Mon. Wea. Rev.,* **126,** 796–811.

——, ——, G. Pellerin, M. Buehner, M. Charron, L. Spacek, and B. Hansen, 2005: Atmospheric data assimilation with an ensemble Kalman filter: Results with real observations. *Mon. Wea. Rev.,* **133,** 604–620.

Huang, X., H. Wang, Y. Chen, X. Zhang, S. Tjernkes, and R. Stuhlmann, 2007: An observing system simulation experiment using both MM5 and WRF: Experiment configuration and preliminary results. *Extended Abstracts, Eighth Annual WRF User's Workshop,* Boulder, CO, University Corporation for Atmospheric Research. [Available online at http://www.mmm.ucar.edu/wrf/users/workshops/WS2007/abstracts/p2-2_Huang.pdf.]

Noilhan, J., and S. Planton, 1989: A simple parameterization of land surface processes for meteorological models. *Mon. Wea. Rev.,* **117,** 536–549.

Parrish, D., and J. Derber, 1992: The National Meteorological Center spectral statistical interpolation analysis system. *Mon. Wea. Rev.,* **120,** 1747–1763.

Rémy, S., and T. Bergot, 2009: Assessing the impact of observations on a local numerical fog prediction system. *Quart. J. Roy. Meteor. Soc.,* **135,** 1248–1265.

Roquelaure, S., and T. Bergot, 2007: Seasonal sensitivity on COBEL-ISBA local forecast system for fog and low clouds. *Pure Appl. Geophys.,* **164,** 1283–1301.

Talagrand, O., R. Vautard, and B. Strauss, 1997: Evaluation of probabilistic prediction systems. *Proc. ECMF Workshop on Predictability,* Reading, United Kingdom, European Centre for Medium-Range Weather Forecasts, 1–26.

Zhang, F., 2005: Dynamics and structure of mesoscale error covariance of a winter cyclone estimated through short-range ensemble forecasts. *Mon. Wea. Rev.,* **133,** 2876–2893.